Flexural-gravity waves generated by different load sizes and configurations on varying ice cover

C. C. Ţugulan [*], O. Trichtchenko[†], E. I. Părău [‡], A. Stevenson [§]

Abstract

Three-dimensional nonlinear flexural-gravity waves generated by moving loads on the surface of an ice cover floating upon water of infinite depth are computed using a boundary integral equation approach. A *hybrid preconditioned Newton-Krylov* (HPNK) method is used to increase the speed of the numerical computations. The effect of variable ice cover, focusing on ridge and channel configuration is investigated. In addition, we consider different distributions of pressure to model the moving loads to determine configurations which lead to smaller deflections, reducing the strain in the ice.

1 Introduction

In many polar regions, such as Northern Canada, frozen bodies of water act as natural, cost-effective alternatives to paved transport routes, providing critical connectivity to remote communities and industry [26]. This network of winter roads, part ice-covered waterways and part terrestrial, enables the transportation of up to a year's worth of critical supplies during their short operational period lasting only a few months [5]. However, the segments built partially over water are becoming increasingly vulnerable to climate change [1], with their yearly lifespan declining due to decreasing ice thickness and consequent load transport restrictions [5, 12, 13, 15]. The response of ice to such transport loads hinges on its properties and load characteristics [3].

The study of hydroelastic waves has a long history, starting with Greenhill [14] (see [30] for an overview). There are many experimental studies in the field investigating the waves generated by moving single or multiple loads with constant or variable speed on floating ice (see e.g. [4, 6, 31]). More recently, these waves have also been observed from satellite [2, 35]. The wave patterns generated by the moving loads have been found using asymptotic methods (see e.g. [8]) and by deriving full dispersive models [9]. More recently, the waves

[*]Department of Physics and Astronomy, The University of Western Ontario
[†]Department of Physics and Astronomy, The University of Western Ontario
[‡]School of Mathematics, University of East Anglia, UK
[§]Department of Physics and Astronomy, The University of Western Ontario

generated by moving loads in a curved trajectory have been investigated by [16]. The deflections and stresses generated by a moving load in a channel of uniform or variable thickness has been studied for the linearised problem [17, 27, 29].

Our work investigates flexural-gravity or hydroelastic waves generated by a moving pressure described by the three-dimensional Euler equations that describe an inviscid, incompressible and irrotational fluid. The effects of a thin ice plate are incorporated as a surface condition within the Bernoulli equation. While many models exist for the flexural term modelling the ice plate [10, 18, 32], we use the linear elastic plate model. We employ a boundary integral formulation, described by Forbes [11] and used later to compute three-dimensional solutions for nonlinear gravity waves [19], capillary-gravity forced [23] and solitary [21, 22] waves, and flexural-gravity waves [20].

In particular, we examine waves generated by a moving load over a floating ice cover, focusing on the spatially varying properties of the ice cover and a variety of load configurations modelled as a pressure distribution. By incorporating a smooth function corresponding to the flexural rigidity of the ice cover, we examine the wave patterns produced for both ridge and channel-type configurations. Further, we investigate how varying the load dimensions or spreading it across multiple loads can reduce the strain induced on the ice, thereby preventing it from fracturing.

With more advances in technology, the problem of computing three-dimensional wave patterns has regained popularity with the application of iterative solvers and preconditioning techniques for modeling ship wakes without ice cover [7, 24] as well as more complex flexural-gravity waves [33]. The work by [33] developed a novel method of treating the flexural term in the equations to efficiently generate the preconditioner for flexural-gravity waves. Our present work aims to exploit the performance gains achieved using the hybrid preconditioned Newton Krylov (HPNK) method [33] to rapidly probe various parameters modelling a wide range of physical conditions.

This paper is organised as follows. In Section 2, we show the set of equations we use to model the waves including models for ice as well as introduce the strain calculations and briefly discuss the computation methods used as these are discussed in [33]. In Section 3, we present the typical wave patterns for ice roads where the flexural rigidity varies and present some sample configurations of pressures that lead to reduced strains. We conclude in Section 4.

2 Formulation

We consider three-dimensional flexural-gravity waves generated by a load moving at speed U in the negative x-direction on top of ice covering water of infinite depth. The load is represented by

$$p(x,y) = \begin{cases} P_0 e^{\frac{L_x^2}{(x^2-L_x^2)} + \frac{L_y^2}{\left(y^2-L_y^2\right)}}, & |x| < L_x \quad \text{and} \quad |y| < L_y \\ 0 \quad \text{otherwise,} \end{cases} \tag{1}$$

where L_x is parallel to direction of travel, L_y is perpendicular to direction of travel, and P_0 represents the mass of the load and its dimensions. Gravity g acts in the negative z-direction, as shown in Figure 1. We assume water is of density ρ and the coefficient of flexural rigidity is given by $D = Eh^3 \big/ 12(1-\nu^2)$, which includes Young's modulus of elasticity E, the Poisson ratio ν, and thickness of the ice sheet h. We use $L = L_y$ as the characteristic length and U as characteristic speed to non-dimensionalise the problem, resulting in the following parameters

$$\epsilon = \frac{P_0}{(\rho U^2)}, \quad F = \frac{gL}{U^2}, \quad \beta = \frac{D}{\rho U^2 L^3}, \tag{2}$$

where ϵ characterizes the strength of the disturbance, F is an inverse length-based Froude number, and β captures the resistance of the ice to bending [20, 32, 33].

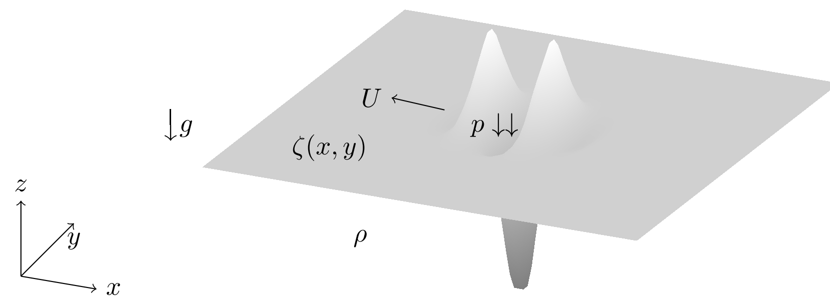

Figure 1: Sketch of the problem with axes and important quantities as labelled.

Assuming the velocity potential is $\Phi(x, y, z)$ and the surface is $z = \zeta(x, y)$ with the schematic given by Figure 1, the non-dimensional Euler equations for an inviscid, incompressible irrotational fluid in a frame of reference moving with the load are

$$\nabla^2\Phi = 0 \text{ on } -\infty < z < \zeta(x, y), \quad \text{and} \quad x, y \in \mathbb{R} \tag{3}$$

$$\Phi_x\zeta_x + \Phi_y\zeta_y = \Phi_z \text{ on } z = \zeta(x, y), \tag{4}$$

$$\frac{1}{2}\left(\Phi_x^2 + \Phi_y^2 + \Phi_z^2\right) + F\zeta + P_{\text{flex}} + \epsilon p = \frac{1}{2} \text{ on } z = \zeta(x, y), \tag{5}$$

$$(\Phi_x, \Phi_y, \Phi_z) \to (1, 0, 0), \quad \zeta \to 0 \quad \text{as} \quad x \to -\infty \tag{6}$$

$$(\Phi_x, \Phi_y, \Phi_z) \to (1, 0, 0), \qquad \text{as} \quad z \to -\infty. \tag{7}$$

The term describing the effects due to the ice cover is given by

$$P_{\text{flex}} = \beta\nabla^4\zeta = \beta(\partial_{xxxx} + \partial_{yyyy} + 2\partial_{xxyy})\zeta. \tag{8}$$

In this work we neglect the inertia of the elastic plate as we are interested in waves whose wavelength is much larger than the ice thickness h. It can be shown that if the thickness of the ice is variable, hence $\beta = \beta(x, y)$, the flexural term can be modelled by

$$P_{\text{flex}} = \nabla^2 \big(\beta \nabla^2 \zeta\big) \approx \beta \nabla^4 \zeta$$

when the variation of β in x and y is small (see e.g. [25]).

2.1 Strain

In the linear thin elastic plate model for ice, assuming the Kirchhoff hypothesis is satisfied, the mid-plane (*i.e.,* halfway through its thickness at $z = h/2$) remains unstrained under subsequent bending [34]. Therefore, the maximum strain at any (x, y) position is located on the surface of the ice, with the most relevant strains being the positive ones corresponding to elongation of the ice surface and tensile stresses within the ice [28]. The strain tensor, which is written in matrix form as equation (9),

$$\varepsilon(x, y) = -\frac{h}{2L}\begin{pmatrix}\zeta_{xx}(x, y) & \zeta_{xy}(x, y)\\ \zeta_{xy}(x, y) & \zeta_{yy}(x, y)\end{pmatrix} = -\frac{h}{2L}\overline{\varepsilon}(x, y). \tag{9}$$

This results in a 2×2 strain tensor describing the state of strain at each point in the profile. Then the maximum strain in the ice sheet is calculated by evaluating the eigenvalues λ_{max} of $\overline{\varepsilon}$ at each location [28], which we refer to as unscaled strain.

2.2 Computational Method

We seek solutions to equations (3) to (7) in a frame of reference moving with the disturbance. We use the boundary-integral equation method [11, 19] where we set the velocity potential on the variable surface equal to $\phi(x, y) = \Phi(x, y, \zeta(x, y))$. resulting in equations provided in [20, 33]. The functions $\zeta(x, y)$ and $\phi(x, y)$ are represented by discrete values $\zeta_{k,\ell}$ and $\phi_{k,\ell}$ evaluated at the mesh points (x_k, y_ℓ) defined by $x_k = x_1 + (k-1)\Delta x$ and $y_\ell = (\ell - 1)\Delta y$ for $k = 1, \dots, N$ and $\ell = 1, \dots, M$, where Δx and Δy are the spacing between mesh points. We choose the first point in the x-direction to be sufficiently upstream so that the waves are assumed to decay to approximately zero amplitude there and we reflect solutions in the $y = 0$ axis of symmetry.

Numerical discretization of these reformulated equations leads to a system of equations that we solve using the hybrid preconditioned Newton-Krylov (HPNK) method developed in [33]. The ordering convention follows [24] wherein the values of the functions $\zeta_{1,\ell}$ and $\phi_{1,\ell}$ at the upstream boundary of the truncated domain are placed before the derivatives $(\phi_x)_{k,\ell}$ and $(\zeta_x)_{k,\ell}$ of the corresponding slice, then the values of ϕ and ζ are obtained via trapezoidal rule integration. This ordering allows us to optimize our scheme to obtain a sparser Jacobian structure as described in [24].

The hybrid method for generating the preconditioner combines the linearised Jacobian of the gravity waves problem (without ice) where each element can be determined analytically, and the flexural contribution capturing the effects due

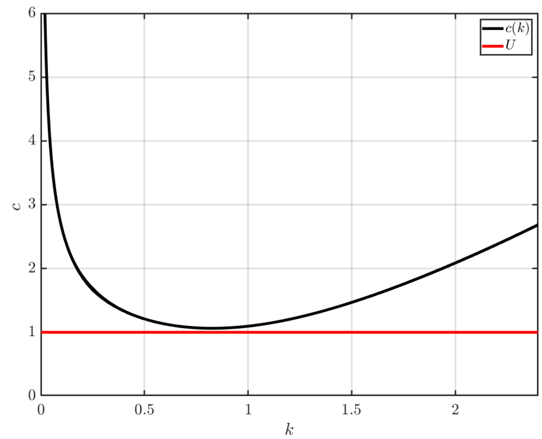

Figure 2: Dimensionless phase speed given by $c = \sqrt{F/k + \beta k^3}$ in black corresponding to $F = 0.7$ and $\beta = 0.5$ with the red line denoting the constant speed of the load $U < c_{min}$.

to the presence of the ice sheet, which is determined numerically using finite differences [33]. The advantage of this approach is that the various physical conditions we are interested in exploring only involve the flexural contribution, which can be computed quickly since it does not involve the nonlocal equations. The analytical formulae are used for all entries of the contribution to the preconditioner without ice (gravity waves) as in [24] and these entries only depend on the parameters of the mesh.

3 Results

We present solutions for flexural-gravity waves generated by a load moving at speed $U < c_{\min}$, where $c_{\min}$ denotes the minimum speed prescribed by the dispersion relation for linear flexural-gravity waves in infinite depth. Using the non-dimensional quantities, it is

$$c_{\min}^2 = \frac{4}{3}\left(3\beta F^3\right)^{\frac{1}{4}}. \tag{10}$$

Figure 2 shows the non-dimensional phase speed in black to $F = 0.7$ and $\beta = 0.5$ with $c_{min} \approx 1.06$ (and $U = 1$). In this regime, we expect localised wave patterns and no waves in the far field, also avoiding resonances between the flexural and gravity contributions.

Our investigation considers the implications of heterogeneous ice properties and diverse load configurations. Firstly, in Section 3.1, we allow for a continuous spatial variation of the ice sheet thickness in the y-direction, *i.e.*, perpendicular to the direction of motion of the load, and assume the load has a length to width ratio of $L_x/L_y = 1$. We use logistic functions to model the properties of the ice and choose parameters corresponding to ridge or channel-type configurations; ice is represented by $\beta = 1$ and open water by $\beta = 0$. Next, in Section 3.2.1, we investigate an uniform ice sheet characterized by $\beta = 0.5$, and explore the responses generated by different load configurations. We consider the case where the individual load length to width ratio L_x/L_y is varied, and the case of dual load configurations (when $L_x/L_y = 1$) in which the loads travel either consecutively or adjacent to each other.

3.1 Non uniform ice plate: varying channel or ridge configurations

We investigate deflection patterns due to a load described by equation (1) with $L_x/L_y = 1$ moving uniformly along the $y = 0$ symmetry axis, when the properties of ice are allowed to vary in space. Different physical or mechanical properties of heterogeneous ice cover can be taken into account, *e.g.,* variable ice thickness, which are reflected through the nondimensionalized flexural rigidity. In Section 2 we have formulated the problem in the frame of reference moving with the load, so to allow for clear interpretation of our travelling wave solutions, we restrict or investigation to varying the properties of the ice cover perpendicular to the direction of motion using the logistic function

$$\beta = \beta(y) = \frac{1}{1 + e^{\gamma\left(y - \frac{y_M}{2} + \sigma\right)}} \in [0, 1] \text{ for } y > 0, \tag{11}$$

reflecting the function about $y = 0$, where γ characterises the steepness of the curve and $(y_M/2 - \sigma)$ is the midpoint defining the transition halfway between solid ice ($\beta = 1$) and open water ($\beta = 0$). Using equation (11), we consider two different configurations representative of a "ridge"($\gamma > 0$) or "channel"($\gamma < 0$) as shown in Figure 3. In our investigation, we observed that the nature of the wave pattern is determined predominantly by the extent of the channel or ridge (see Figure 3) which is determined by the parameter σ. As such, we consider a fixed slope and range for $\beta(y) \in [0, 1]$ and vary the dominant parameter σ. Note that we have assumed symmetry about $y = 0$ for $\beta(y)$ which may not always be physically realistic. Since the goal was to compare with previous work for homogeneous ice as in [32, 33], we also used the same symmetry to obtain results with similar resolution and mesh sizes for varying $\beta(y)$. However, this restriction does not have to be made and any $\beta(y)$ can be used with the methods shown in this work.

In considering the ridge-type configurations shown in Figure 3a with $\gamma = 3$ and $\sigma = -4, 0, 4, 8$, we obtain the wave patterns shown in Figures 4a - 4d where we see that the effect of gradually narrowing the width of the ridge leads to a transition between a compact wave pattern, typical to waves under ice for $U < c_{\min}$, to one that resembles a Kelvin wake in open water. The three-dimensional solutions were computed on a mesh size of 121×61 with uniform grid-spacing $\Delta x = \Delta y = 10/31$.

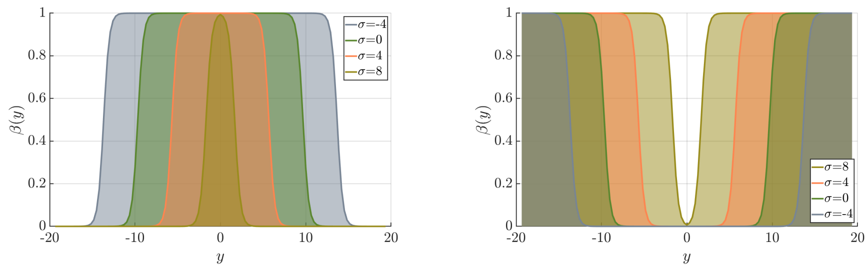

(a) Ridge functions with $\gamma = 3$

(b) Channel functions with $\gamma = -3$

Figure 3: Varying flexural rigidity $\beta(y)$ with $\gamma = \pm 3$, $\sigma = -4, 0, 4, 8$.

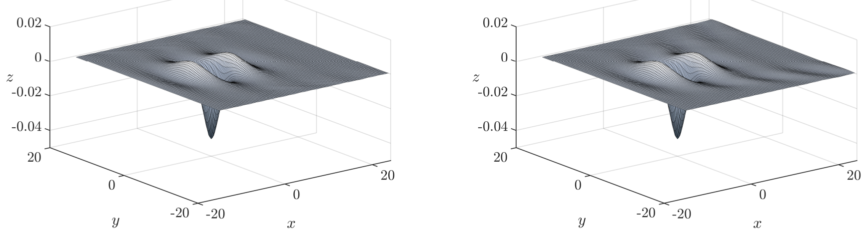

(a) $\sigma = -4$

(b) $\sigma = 0$

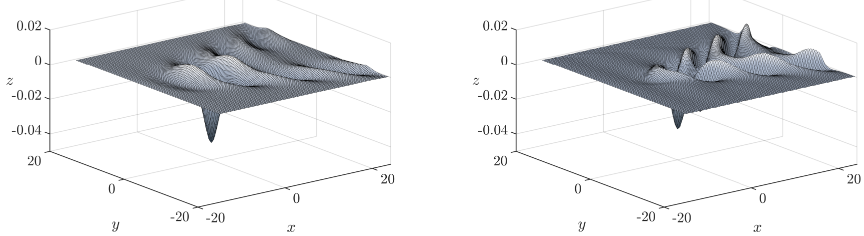

(c) $\sigma = 4$

(d) $\sigma = 8$

Figure 4: Flexural-gravity waves for $U < c_{\min}$ computed on a 121×61 mesh with spacing $\Delta x = \Delta y = 10/31$ and dimensionless $F = 0.7$, for a pressure distribution with $L_x/L_y = 1$ and $\epsilon = 1$ where we model a ridge with $\gamma = 3$, $\sigma = 0, 4, 6, 8$.

Next, we consider the channel-type configurations shown in Figure 3b using $\gamma = -3$ and varying $\sigma = -4, 0, 4, 8$ in equation (11). The corresponding three-dimensional surface profiles in Figures 5a-5d show the effect of varying the width of the channel on wave patterns. These wave patterns transition between something resembling a Kelvin wake behind a moving pressure as in Figure 5a, through a more complicated pattern as in Figure 5c, to an almost periodic train of waves in the x direction as in 5d. This can be explained by considering that in the limit of a very narrow channel, the y direction becomes unimportant so only variations in x remain.

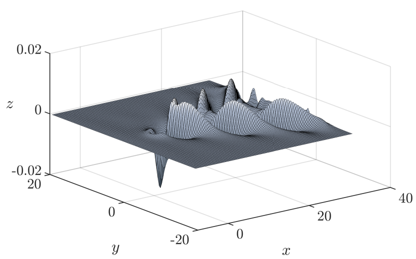

(a) $\sigma = -4$

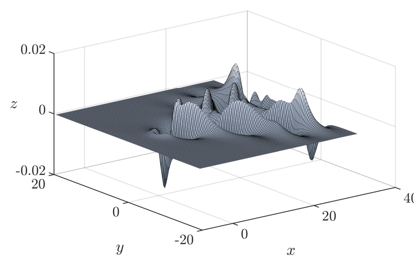

(b) $\sigma = 0$

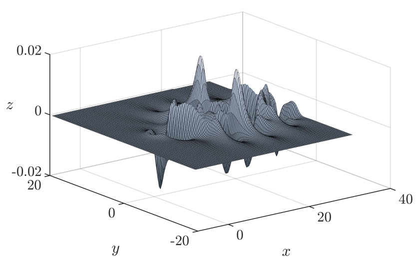

(c) $\sigma = 4$

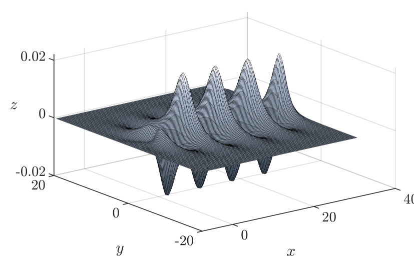

(d) $\sigma = 8$

Figure 5: Flexural-gravity waves computed on a 121×61 mesh with spacing $\Delta x = \Delta y = 10/31$ and in the regime $U < c_{\min}$ with $F = 0.7$ generated by a pressure with $L_x/L_y = 1$ and $\epsilon = 0.1$. Channel parameters are $\gamma = -3$ and $\sigma = -4, 0, 4, 8$, with $\sigma = 8$ the most narrow.

It is worth mentioning that other variations in $\beta(y)$ functions were also tested, for example considering a sinusoidal variation. However, it was found that this did not lead to quantitatively different wave profiles even if the period or amplitude of the function were varied. Instead, the wave patterns resembled those that would be obtained for a constant $\beta(y)$ which would take on the value of the average of the sinusoidally varying function.

3.2 Uniform ice plate: varying load configuration

3.2.1 Varying individual load dimensions

In this section, we consider the effect of varying the dimensions a load of mass Ms, assuming a localised form of the pressure given by equation (1). Due to our non-dimensionalisation, $L = L_y = 1$ and we investigate the effect of varying the length of the load L_x via the ratio L_x/L_y. To keep the vertical force exerted by the moving load on ice constant $|\mathbf{F}| := \int\int_A p(x,y)dA = Mg$ we obtain

$$|\mathbf{F}| = \int_{-L_x}^{L_x}\int_{-L_y}^{L_y} P_0 e^{\frac{L_x^2}{x^2-L_x^2}} e^{\frac{L_y^2}{y^2-L_y^2}}\,\mathrm{d}x\,\mathrm{d}y = P_0 L_x L_y \left(\int_{-1}^{1} e^{\frac{1}{t^2-1}}\,\mathrm{d}t\right)^2$$
$$\approx P_0 L_x L_y 0.197131.$$

So, for a moving load of mass M,

$$\epsilon = \frac{P_0}{\rho U^2} = \frac{Mg}{L_x L_y}\cdot\frac{1}{0.197131}\cdot\frac{1}{\rho U^2}. \tag{12}$$

We impose the mass of the load to remain constant as the length of the load is varied. We normalise the pressure distribution as shown in Figure 6 depicting the centrelines $p(x,0)$ of the different pressure distributions examined for $L_x/L_y = 1, 2, 6, 12, 23.52$, where the value $L_x/L_y = 23.52$ for the chosen domain corresponds to the pressure spanning 98% of the domain in the x-direction.

All solutions presented were computed on a 160×80 mesh with uniform spacing $\Delta x = \Delta y = 0.3$ and $x_0 = -24$ on a domain symmetric in y. We assume that the load is moving in the $U < c_{\min}$ regime (where only a localised response is predicted), using the dimensionless parameters $F = 0.7$ and $\beta = 0.5$.

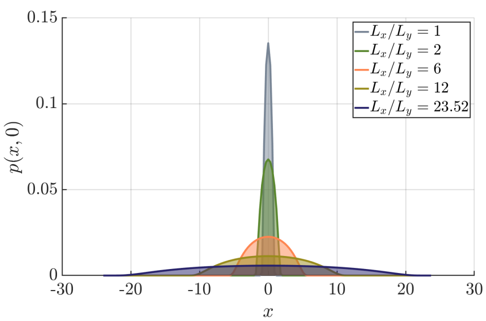

Figure 6: Centrelines of pressure distribution $p(x,0)$ for varying L_x/L_y.

Three-dimensional forced wave solutions for the surface profiles in Figure 7 show that that the pattern remains localised as the length of the load is varied with $L_x/L_y = 1, 6, 12, 23.52$. The base case $L_x/L_y = 1$ for a load with equal length and width is shown in Figure 7a. We see that as the length of the load increases, the maximum amplitude of the depression decreases as expected since the pressure distribution is applied over a larger area. We note that the solution in Figure 7d with $L_x = 23.52$ converges to the same wave profile when the length of the computational domain was extended in the x-direction.

The centreline plots in Figures 8a and 8b provide a clear comparison of solutions for different L_x/L_y ratios which illustrates the decrease in the maximum amplitude of depression as the value of L_x/L_y is increased. Consequentially,

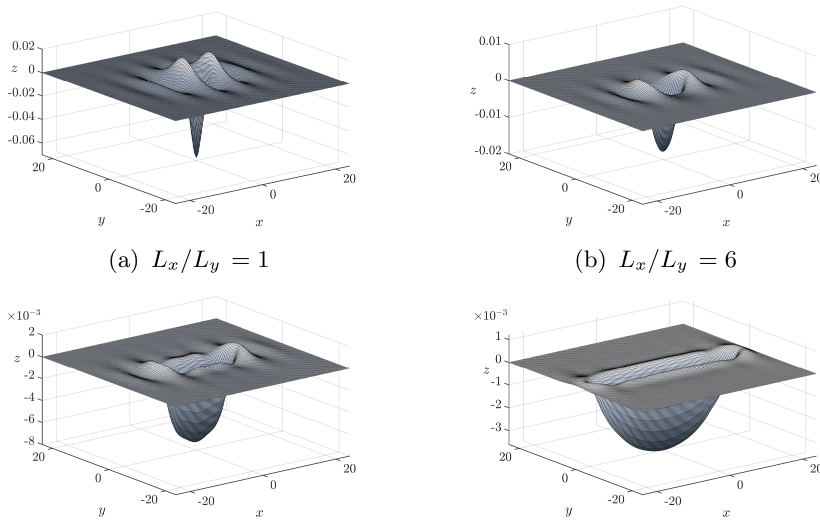

(a) $L_x/L_y = 1$ (b) $L_x/L_y = 6$

(c) $L_x/L_y = 12$ (d) $L_x/L_y = 23.52$

Figure 7: Flexural-gravity waves computed a 160×80 mesh with uniform grid spacing $\Delta x = \Delta y = 0.3$ for load distributions with $L_x/L_y = 1, 2, 6, 12, 23.52$. As L_x increases, the maximum amplitude of the depression decreases.

the reduction in the maximum amplitude of depression corresponds to a decrease in the maximum absolute eigenvalue $\max\limits_{k,l} |\lambda(x_k, y_l)|$ of the strain tensor equation (9) evaluated at each (x_k, y_ℓ) point on the domain as shown in Figure 9. Please note that for simplicity, we present in this figure and the following ones the unscaled strain $\bar{\varepsilon}$ which needs to be multiplied by $h/2L$ to obtain the physical strain ε.

Interestingly, as we increase the L_x/L_y ratio, in Figure 9 we find that the absolute magnitude of the maximum eigenvalues decays towards zero. As this decrease in strain can be shown to fit an exponential decay, this means that when the load distribution is $L_x/L_y = 12$, the strain has already decreased to less than 90% of the original value, so any further increase in L_x/L_y will have diminishing effects on the value of strain.

3.2.2 Multiple pressure distributions

Finally, we consider what happens if the load is modelled by a linear combination of the pressure distributions p_n centered at the points $(x, y) = (x_n, y_n)$ defined

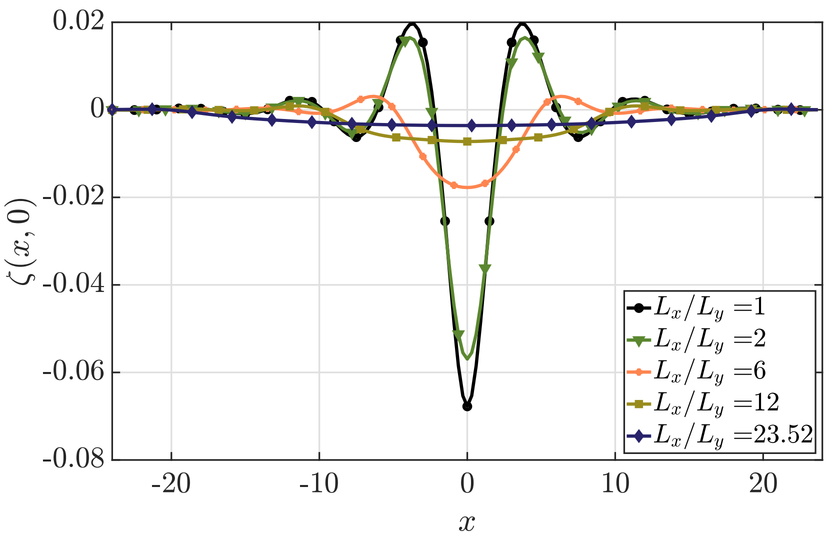

(a) $\zeta(x,0)$ centrelines

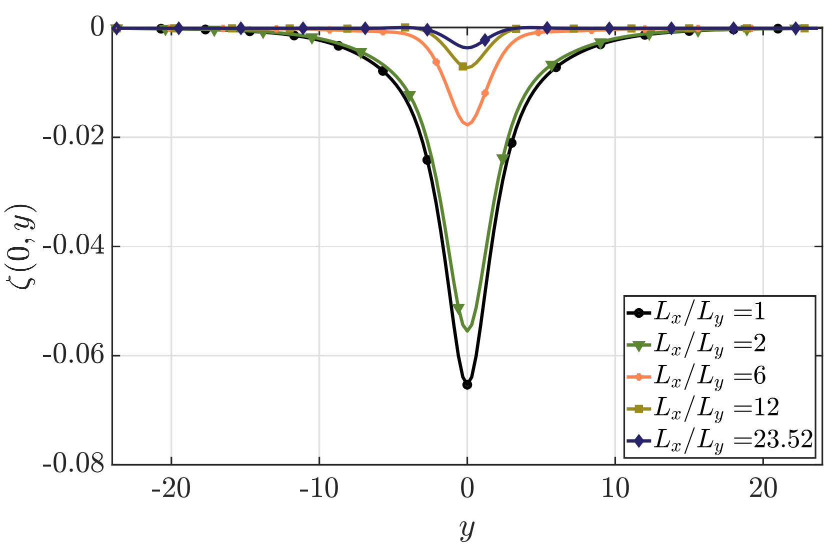

(b) $\zeta(0,y)$ centrelines

Figure 8: Centrelines shown for $L_x/L_y = 1, 2, 6, 12, 23.54$.

by

$$p_n(x,y) = \begin{cases} \epsilon_n e^{\frac{L_x^2}{((x-x_n)^2 - L_x^2)} + \frac{L_y^2}{((y-y_n)^2 - L_y^2)}}, & |x - x_n| < L_x, |y - y_n| < L_y \\ 0 \quad \text{otherwise.} \end{cases} \tag{13}$$

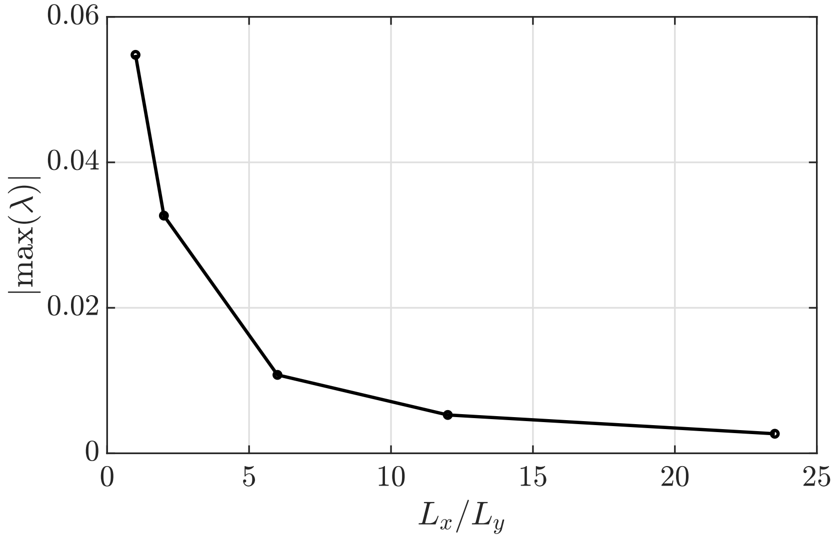

Figure 9: Plot of the maximum eigenvalue λ for the unscaled strain for different pressure distributions with varying $L_x/L_y = 1, 2, 6, 12, 23.52$. computed on a 160×80 mesh with $\Delta x = \Delta y = 0.3$.

We consider dual load configurations where both loads have the same mass (*i.e.,* $\epsilon_1 = \epsilon_2 = 1$) and length to width ratio $L_x/L_y = 1$.

We first explore consecutive loads travelling along the $y = 0$ axis with the same uniform speed $U < c_{\min}$. The total pressure distribution for the dual load configuration centred about the origin is defined using equation (13) by $p(x, y) = p_1(x, y; x_1, 0, \epsilon_1)+p_2(x, y; x_2, 0, \epsilon_2)$ where $x_1 = -x_2$ such that the loads maintain a distance $d = x_2 - x_1$ from one another. The wave patterns for two consecutive loads travelling at various separation distances $d = 0, 2, 4, 8, 10, 12$ are shown in Figures 10a - 10f.

The trivial case shown in Figure 10a with $d = 0$ corresponds to doubling ϵ for an individual load, which results in a larger amplitude of deflection. Figure 10b shows the response when $d = 2$, representing the scenario in which two loads are “attached”in the sense that the tails of their individual pressure distributions (p_1 and p_2) are slightly overlapping.

As we increase the distance between the pressure distributions, we observe destructive and constructive interference pattern. In the case of Figure 10c, destructive interference leads to the smallest wave amplitude for the separations considered, which suggests this is an ideal load distribution for minimizing the deflections in ice. Conversely, Figure 10d, shows the waves generating by moving pressures for $d = 8$ can constructively interfere and potentially lead to a larger strain. The maximum amplitudes of the depressions produced by two loads travelling at distances beyond $d = 12$ shown in Figure 10f approximate that of an individual load since the localised wave pattern produced by each load no longer interact. Comparisons of these surface profiles are depicted by the centrelines in Figure 11a and Figure 11b.

Analysing the eigenvalues λ of the unscaled strain tensor given in equation (9) for different separation distances between the pressures travelling one after the other, we obtain the results shown in Figure 12. We observe that for a separation of $d = 3$ we obtain the smallest unscaled strain, which corresponds to the regime in which the two pressures maximally destructively interfere. For $d = 0$, the eigenvalue is almost twice the case when there is only one pressure (≈ 0.55) as seen in Figure 9 for $L_x = L_y = 1$. Overall, the successive maxima and minima corresponding to constructive and destructive interference decay in amplitude as the load separation distance is increased, to the case where the load is applied in only one place. This implies there are ways to distribute the load that can decrease or increase the strain on ice.

We also consider pressure distributions modelling two loads travelling side-by-side by defining the forcing term as $p(x, y) = p_0(x, y; 0, y_0, \epsilon_0)$ using equation (13) such that each load is at a distance of y_0 from the origin and total distance of $d = 2y_0$ from one another. As in the y direction the wave profile only contains a maximum, there is no destructive, only constructive interference. We include one sample wave profile with $d = 12$ in Figure 13 and the strain simply decays to the case where the wave profiles from each pressure no longer interact, as shown in Figure 15.

We have also varied the mass of each load either travelling side by side or one after the other. The plots representing the maximum eigenvalues do not look qualitatively different from Figures 12 and 15. The only difference is that if one load is smaller than the other, then the effects of constructive or destructive interference are less pronounced so we do not include those results in this paper.

4 Conclusion

In this work, we have employed the HPNK method to efficiently compute solutions for flexural-gravity waves, generated by a load moving across a floating ice cover in the subcritical speed regime under different conditions. We have considered the influences of variable ice properties and different load configurations, using a logistic function to represent ridge or channel-type configurations. Using a uniform ice cover, we explored the effect of varying the length to width ratio for an individual load, and considered dual load configurations for scenarios in which two identical loads are moving consecutively or adjacently in the same direction at various separation distances. For the results involving uniform ice cover, maximum eigenvalues of the strain tensor were also computed to understand under which conditions the strain could be minimized. Our work can be used to infer safety regimes by calculating the strains in various configurations.

In the cases where nonuniform ice cover was considered, the results in Section 3.1 showed the emergence of a Kelvin wake pattern as the width of the ridge was decreased, while in the narrow channel case the wave pattern approached a

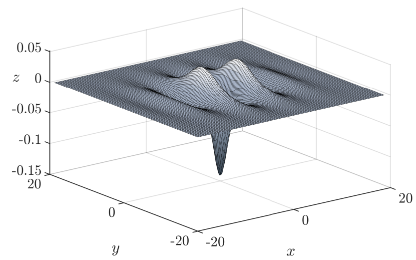

(a) $d = 0$

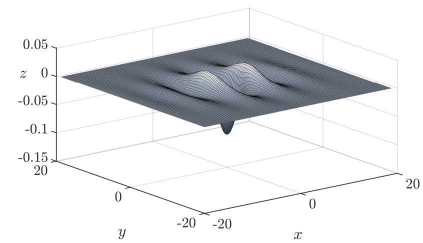

(b) $d = 2$

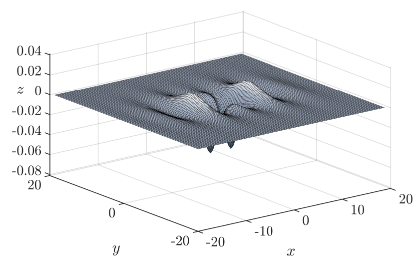

(c) $d = 4$

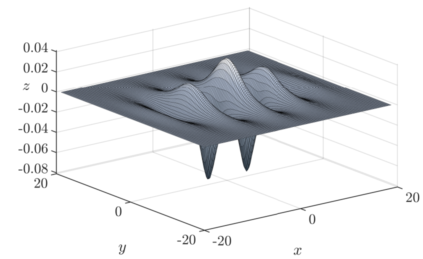

(d) $d = 8$

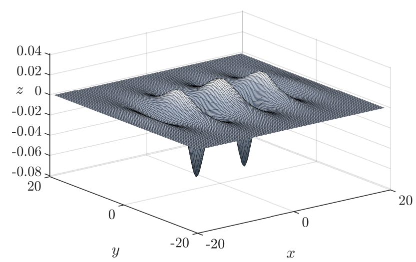

(e) $d = 10$

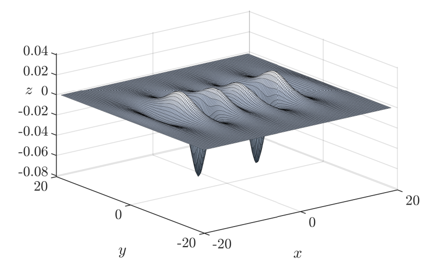

(f) $d = 12$

Figure 10: Forced wave solutions computed a 121×61 mesh with uniform grid spacing $\Delta x = \Delta y = 10/31$ for loads moving one behind another at different separation distances $d = 0, 2, 4, 8, 10, 12$

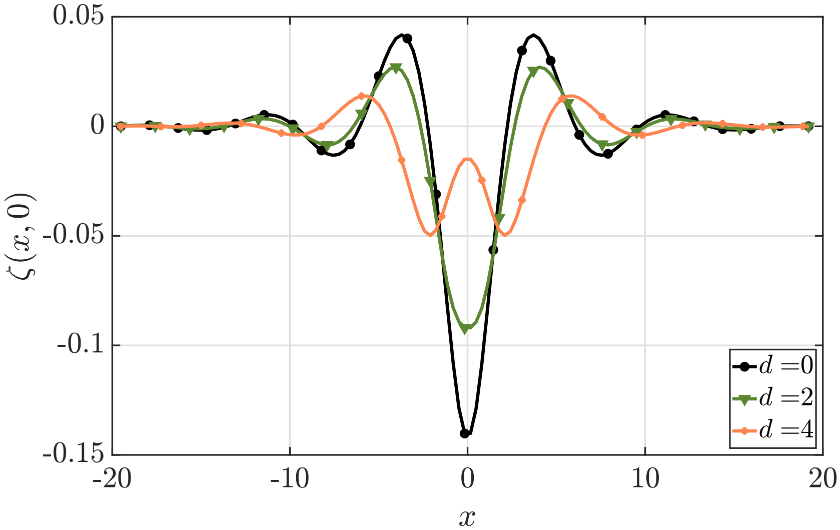

(a) $\zeta(x,0)$ centrelines for $d = 0, 2, 4$

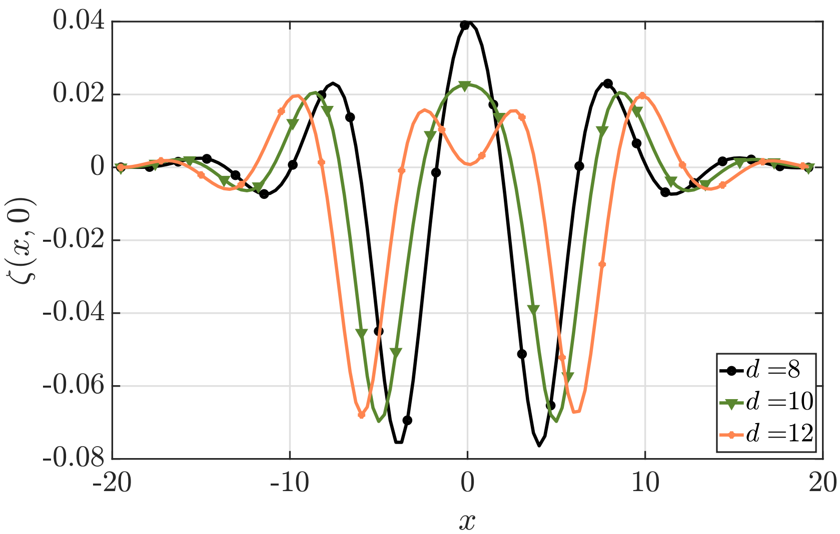

(b) $\zeta(x,0)$ centrelines for $d = 8, 10, 12$

Figure 11: Centrelines shown for various separation distances with the pressure distributions one behind another.

two-dimensional wave profile with an almost periodic train of waves behind the pressure. For a uniform ice cover, the results in Section 3.2.1 illustrated that the effect of increasing the load length while mass was fixed, yielded the expected

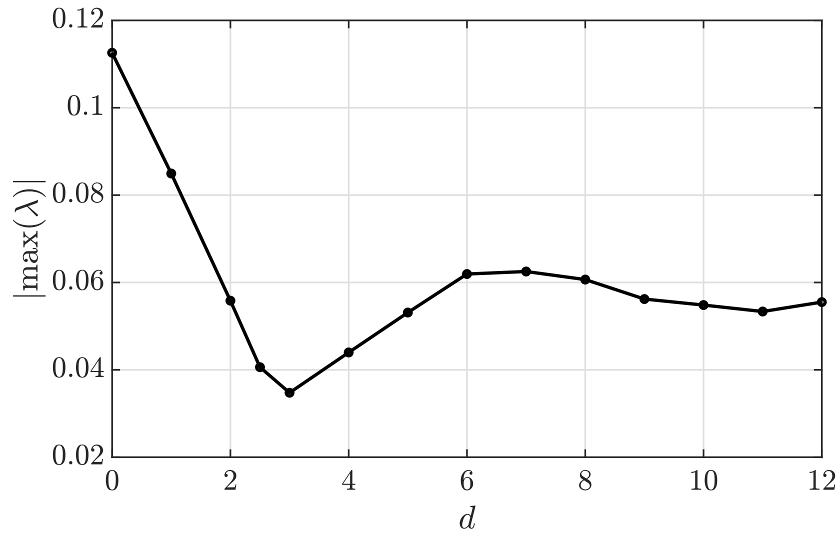

Figure 12: Plot of maximum eigenvalues corresponding to principal strain states for pressure distributions travelling one behind another at various distances computed on a 121×61 mesh with $\Delta x = \Delta y = 10/31$.

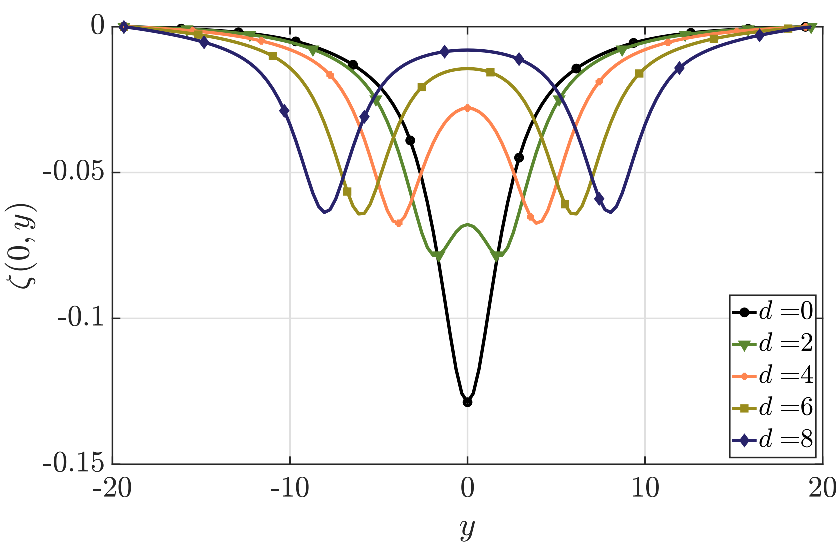

Figure 13: Centrelines shown for various separation distances with the pressure distributions travelling side-by-side.

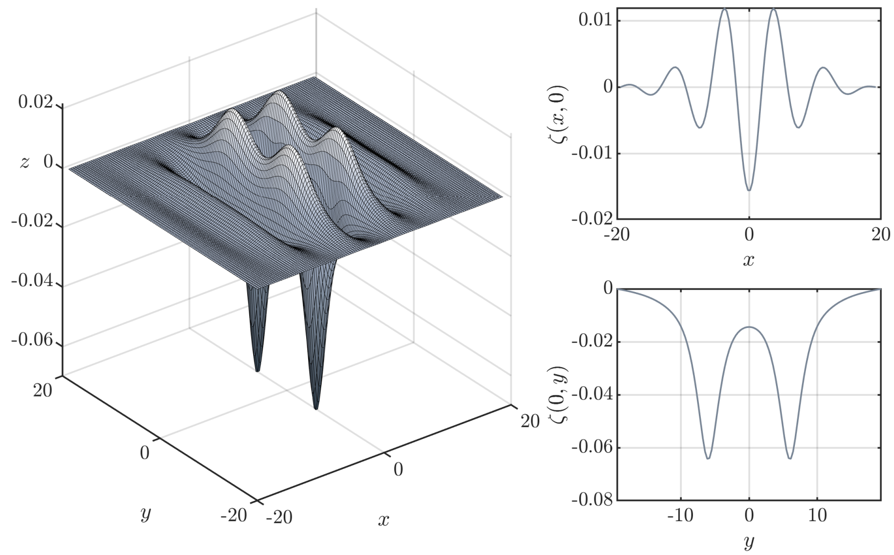

Figure 14: Solution for $p = \epsilon_1 p_1(0,6)$ reflected in the axis of symmetry, corresponding two identical loads travelling side-by-side where $\Delta x = \Delta y = 10/31$ and $L_x/L_y = 1$, $\epsilon_1 = 1$.

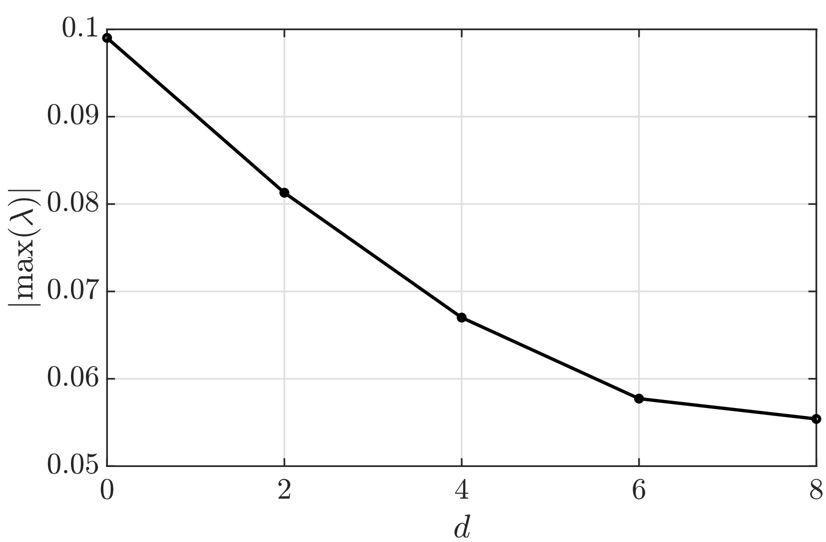

Figure 15: Plot of maximum eigenvalues corresponding to principal strain states for pressure distributions travelling beside each other at various distances $d = 0, 2, 4, 6, 8$ computed on a 121×61 mesh with $\Delta x = \Delta y = 10/31$.

decrease in the maximum amplitude of the depression, given the larger area over which the pressure was distributed. Consequentially, the unscaled strain decayed towards zero as the length was increased, suggesting a critical load length L_x where distributing the load over a larger length minimally affected the strain on the ice cover.

In the dual load configuration involving consecutively moving loads, we observed constructive or destructive interference between the wave patterns produced by each load depending on their separation distance. Beyond the largest separation distance, the maximum absolute eigenvalue of the strain tensor approximated that of a single load. These results suggested certain load separation distances are more effective than others for minimising strain on the ice cover. In contrast, for two adjacently moving loads, we found no destructive interference due to the absence of alternating maxima and minima in the y-direction, perpendicular to the motion of the load. Consequently, the maximum strain-related eigenvalue decayed to that of a single, independently travelling load as the separation distance increased.

References

[1] H. Babaei and P. D. Barrette. A computational modeling basis in support of the canadian winter road infrastructure. Technical report, National Research Council Canada, 2020.

[2] H. Babaei, J. Van Der Sanden, N. Short, and P. D. Barrette. Lake ice cover deflection induced by moving vehicles: comparing theoretical results with satellite observations. *Proceedings of TAC*, 2016.

[3] P. D. Barrette. A review of guidelines on ice roads in canada: Determination of bearing capacity. In *TAC 2015: Getting You There Safely-2015 Conference and Exhibition of the Transportation Association of Canada*, 2015.

[4] P. D. Barrette. *On the reinforcement of ice covers for surface transportation*. National Research Council Canada= Conseil national de recherches Canada, 2021.

[5] P. D. Barrette, Y. Hori, and A. M. Kim. The canadian winter road infrastructure in a warming climate: Toward resiliency assessment and resource prioritization. *Sustainable and Resilient Infrastructure*, 7(6):842–860, 2022.

[6] S. Beltaos. Field studies on the response of floating ice sheets to moving loads. *Canadian Journal of Civil Engineering*, 8(1):1–8, 1981.

[7] N. R. Buttle, R. Pethiyagoda, T. J. Moroney, and S. W. McCue. Three-dimensional free-surface flow over arbitrary bottom topography. *Journal of Fluid Mechanics*, 846:166–189, 2018.

[8] J.W. Davys, R.J. Hosking, and A.D. Sneyd. Waves due to a steadily moving source on a floating ice plate. *Journal of Fluid Mechanics*, 158:269–287, 1985.

[9] E. Dinvay, H. Kalisch, and E. I. Părău. Fully dispersive models for moving loads on ice sheets. *Journal of Fluid Mechanics*, 876:122–149, 2019.

[10] L. K. Forbes. Surface waves of large amplitude beneath an elastic sheet. part 2. galerkin solution. *Journal of Fluid Mechanics*, 188:491–508, 1988.

[11] L. K. Forbes. An algorithm for 3-dimensional free-surface problems in hydrodynamics. *Journal of Computational Physics*, 82(2):330 – 347, 1989.

[12] L. W. Gold. Field study on the load bearing capacity of ice covers. *Pulp and Paper in Canada*, 61(5):153–8, 1960.

[13] L. W. Gold. Use of ice covers for transportation. *Canadian Geotechnical Journal*, 8(2):170–181, 1971.

[14] A. G. Greenhill. Wave motion in hydrodynamics. *American Journal of Mathematics*, 9(1):62–96, 1886.

[15] Y. Hori, W. A. Gough, K. Butler, and L. J. S. Tsuji. Trends in the seasonal length and opening dates of a winter road in the western james bay region, ontario, canada. *Theoretical and Applied Climatology*, 129(3):1309–1320, 2017.

[16] K.R. Johnsen, H. Kalisch, and E. I. Părău. Ship wave patterns on floating ice sheets. *Scientific Reports*, 12(1):18931, 2022.

[17] T. Khabakhpasheva, K. Shishmarev, and A. Korobkin. Large-time response of ice cover to a load moving along a frozen channel. *Applied Ocean Research*, 86:154–165, 2019.

[18] P. A. Milewski and Z. Wang. Three dimensional flexural–gravity waves. *Studies in Applied Mathematics*, 131(2):135–148, 2013.

[19] E. I. Părău and J.-M. Vanden-Broeck. Nonlinear two- and three-dimensional free surface flows due to moving disturbances. *European Journal of Mechanics - B/Fluids*, 21(6):643–656, Nov 2002.

[20] E. I. Părău and J.-M. Vanden-Broeck. Three-dimensional waves beneath an ice sheet due to a steadily moving pressure. *Philosophical Transactions: Mathematical, Physical and Engineering Sciences*, 369(1947):2973–2988, 2011.

[21] E. I. Părău, J.-M. Vanden-Broeck, and M. J. Cooker. Nonlinear three-dimensional gravity-capillary solitary waves. *Journal of Fluid Mechanics*, 536:99–105, 2005.

[22] E. I. Părău, J.-M. Vanden-Broeck, and M. J. Cooker. Three-dimensional gravity-capillary solitary waves in water of finite depth and related problems. *Physics of Fluids*, 17(12):122101, 2005.

[23] E. I. Părău, J.-M. Vanden-Broeck, and M. J. Cooker. Three-dimensional capillary-gravity waves generated by a moving disturbance. *Physics of fluids (1994)*, 19(8):82–102, 2007.

[24] R. Pethiyagoda, S. W. McCue, T. J. Moroney, and J. M. Back. Jacobian-free Newton–Krylov methods with GPU acceleration for computing nonlinear ship wave patterns. *Journal of Computational Physics*, 269:297–313, 2014.

[25] D. Porter and R. Porter. Approximations to wave scattering by an ice sheet of variable thickness over undulating bed topography. *Journal of Fluid Mechanics*, 509:145–179, 2004.

[26] T. D. Prowse, C. Furgal, R. Chouinard, H. Melling, D. Milburn, and S. L. Smith. Implications of climate change for economic development in northern canada: Energy, resource, and transportation sectors. *AMBIO: A Journal of the Human Environment*, 38(5):272–281, 2009.

[27] K. Shishmarev, T. Khabakhpasheva, and A. Korobkin. The response of ice cover to a load moving along a frozen channel. *Applied Ocean Research*, 59:313–326, 2016.

[28] K. Shishmarev, T. Khabakhpasheva, and A. Korobkin. The response of ice cover to a load moving along a frozen channel. *Applied Ocean Research*, 59:313–326, 2016.

[29] K. Shishmarev, T. Khabakhpasheva, and K. Oglezneva. Steady-state motion of a load on an ice cover with linearly variable thickness in a channel. *Journal of Marine Science and Engineering*, 11(5):1045, 2023.

[30] V. A. Squire. Of ocean waves and sea-ice revisited. *Cold Regions Science and Technology*, 49(2):110–133, 2007.

[31] T. Takizawa. Response of a floating sea ice sheet to a steadily moving load. *Journal of Geophysical Research: Oceans*, 93(C5):5100–5112, 1988.

[32] O. Trichtchenko, E. I. Părău, J.-M. Vanden-Broeck, and P. A. Milewski. Solitary flexural–gravity waves in three dimensions. *Philosophical Transactions of the Royal Society A: Mathematical, Physical and Engineering Sciences*, 376(2129):20170345, 2018.

[33] C. C. Ţugulan, O. Trichtchenko, and E. I. Părău. Three-dimensional waves under ice computed with novel preconditioning methods. *Journal of Computational Physics*, 459:111129, 2022.

[34] A. C. Ugural. *Stresses in Plates and Shells*. McGraw-Hill, 1981.

[35] J.J. Van der Sanden and N.H. Short. Radar satellites measure ice cover displacements induced by moving vehicles. *Cold Regions Science and Technology*, 133:56–62, 2017.